Out-of-Plane Alignment of Er(trensal) Easy Magnetization Axes Using Graphene

Jan Dreiser,*[†,‡] Giulia E. Pacchioni,[‡] Fabio Donati,[‡] Luca Gragnaniello,[‡,¶] Alberto Cavallin,[‡] Kasper S. Pedersen,[§] Jesper Bendix,[⊥] Bernard Delley,[∥] Marina Pivetta,[‡] Stefano Rusponi,[‡] and Harald Brune[‡]

[†]Swiss Light Source and [∥]Condensed Matter Theory, Paul Scherrer Institut, 5232 Villigen, Switzerland
[‡]Institute of Physics, Ecole Polytechnique Fédérale de Lausanne, 1015 Lausanne, Switzerland
[§]CNRS, CRPP, UPR 8641 and CNRS, ICMCB, UPR 9014, 33600 Pessac, France
[⊥]Department of Chemistry, University of Copenhagen, 2100 Copenhagen, Denmark

Ⓢ *Supporting Information*

ABSTRACT: We have studied Er(trensal) single-ion magnets adsorbed on graphene/Ru(0001), on graphene/Ir(111), and on bare Ru(0001) by scanning tunneling microscopy and X-ray absorption spectroscopy. On graphene, the molecules self-assemble into dense and well-ordered islands with their magnetic easy axes perpendicular to the surface. In contrast, on bare Ru(0001), the molecules are disordered, exhibiting only weak directional preference of the easy magnetization axis. The perfect out-of-plane alignment of the easy axes on graphene results from the molecule–molecule interaction, which dominates over the weak adsorption on the graphene surface. Our results demonstrate that the net magnetic properties of a molecular submonolayer can be tuned using a graphene spacer layer, which is attractive for hybrid molecule–inorganic spintronic devices.
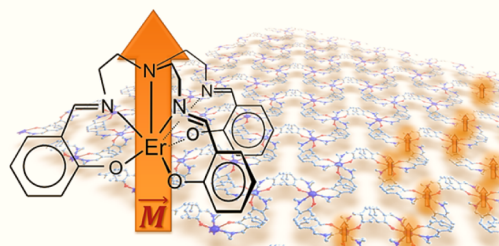
KEYWORDS: *single-ion magnets, single-molecule magnets, surfaces, graphene, magnetic anisotropy, self-assembly*

Single-molecule magnets[1–3] (SMMs) are attractive candidates for molecular spintronics,[4,5] which can be realized in the form of hybrid molecule–inorganic systems.[6] Their mononuclear versions, also termed single-ion magnets (SIMs), possess interesting magnetic properties similar to those of SMMs with larger magnetic units. In addition, structural stability of SIMs facilitates vacuum sublimation, opening the door to binding them to an enormous variety of possible substrates. Lanthanide ions are heavily used as magnetic centers in SIMs[7–9] because of their large magnetic moments and magnetic anisotropies. The Er(trensal)[10–13] SIM is of particular interest here since it exhibits excellent optical fluorescence properties,[10] strong magnetic anisotropy,[11,13] and a trigonal pyramidal structure that allows for several possible adsorption conformations[14] that are difficult to obtain with planar molecules. To organize the molecules on the surface, it is possible to exploit molecular self-assembly, which allows for the bottom-up production of perfect, large-scale samples. It has been demonstrated that the use of atomic monolayer-thick decoupling layers such as graphene (G)[15–18] or hexagonal boron nitride (h-BN)[15,19–21] grown on metal substrates can lead to a reduction of the molecule–surface interaction, promoting molecular self-assembly[22–26] as well as template-directed assembly.[22,27–29] From the viewpoint of magnetism, studies involving decoupling layers have so far been limited to

planar metal–phthalocyanines and metalloporphyrins.[23–25,30–35] More complex molecules have been almost completely neglected, with very few exceptions, such as the prototype SMM Mn_{12}-ac as well as a derivative of the Fe_4 SMM on h-BN/Rh(111)[36,37] and Cu_2N.[38] However, a direct study of the alignment of the magnetic anisotropy easy axes is missing.

Here we show that the molecular self-assembly and orientation of the magnetic easy axes of tripodal Er(trensal) SIMs can be effectively controlled using G decoupling layers grown on Ru(0001) and Ir(111) single-crystal surfaces. In particular, using the G layers, we achieve a perfect alignment of the magnetic easy axes perpendicular to the surface. We employ scanning tunneling microscopy (STM), X-ray absorption spectroscopy (XAS), and X-ray magnetic circular dichroism (XMCD) in order to characterize the structure and magnetism of the submonolayers of adsorbed molecules. The molecules deposited on the bare Ru(0001) exhibit a random distribution of adsorption sites as well as several different adsorption conformations. Consistently, the molecular ensemble only possesses a very weak net magnetic anisotropy despite the
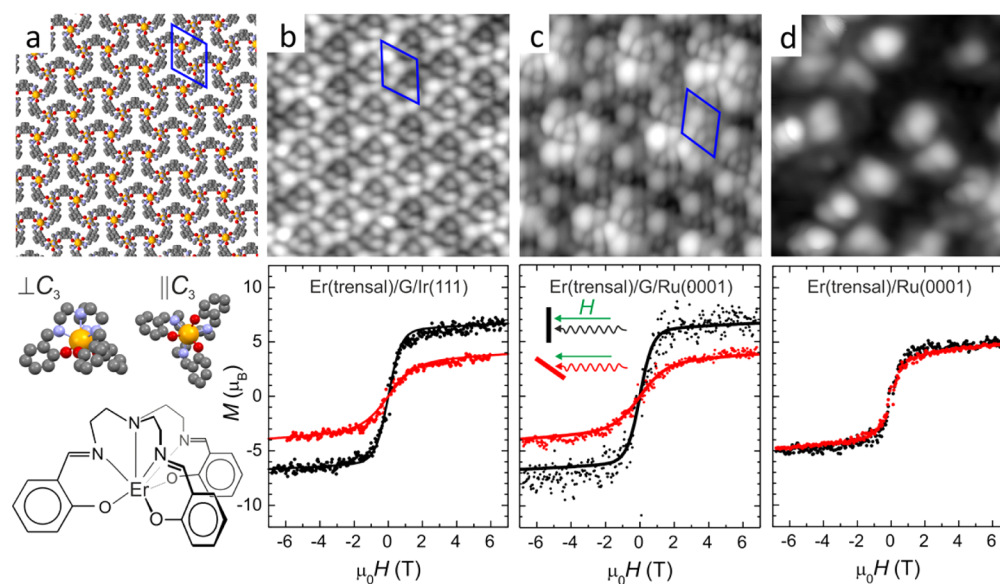
Figure 1. (a) Single layer of the bulk crystalline molecular lattice normal to the crystalline and molecular C_3 axis (*ab* plane), with the phenyl rings of the molecules pointing up and down in an alternating fashion. Structural views and scheme of the Er(trensal) molecule. Color code: orange, Er; blue, N; red, O; gray, C; H atoms have been omitted for clarity. (b–d) STM images (8×8 nm^2) and Er $M(H)$ from XMCD at 3 K in normal ($\theta = 0°$) and grazing incidence ($\theta = 65°$) geometry. Nominal coverages of Er(trensal) were 0.25 to 0.30 ML. In (a–c), the unit cell is shown in blue. (b) Er(trensal)/G/Ir(111), $V_t = -2.5$ V, $I_t = 30$ pA; (c) Er(trensal)/G/Ru(0001), $V_t = -2.5$ V, $I_t = 30$ pA; and (d) Er(trensal)/Ru(0001), $V_t = -0.02$ V, $I_t = 50$ pA. In the magnetization curves, experimental data are plotted as symbols, and solid lines in (b,c) represent calculations using the spin-Hamiltonian of Er(trensal) bulk single crystals.

strong uniaxial magnetic anisotropy of the individual molecules. In contrast, the employment of a G interlayer leads to the formation of self-assembled and oriented islands of Er(trensal) molecules. Within the islands, the molecules are organized as in the bulk molecular crystal, and their magnetic easy axes are aligned perpendicular to the substrate surface. In line with this finding, the molecular ensemble on G exhibits a strong net magnetic anisotropy. While the azimuthal orientation of the molecules within each island is well-defined, there is no such preferred orientation of the islands with respect to the G layers. Furthermore, the stronger periodic corrugation of G/Ru(0001) as compared to G/Ir(111) has no influence on the self-assembly of the molecules.

RESULTS AND DISCUSSION

The structure of the Er(trensal) molecules known from single-crystal X-ray diffraction is shown in Figure 1a along with a single layer of molecules parallel to the densely packed *ab* plane of the molecular crystal. In this arrangement, the molecular C_3 axes are perpendicular to the *ab* plane. The seven-coordinated Er(III) ion is located at the C_3 symmetric site, with the ligand exhibiting three legs formed out of slightly tilted phenyl rings. This tilt gives rise to a three-lobe propeller-like chiral, neutral complex. The molecular C_3 axis coincides with the magnetic easy axis. In the *ab* plane, the molecules are arranged in an alternating fashion, having their nearest neighbors oriented in the opposite direction with their phenyl rings alternatingly pointing up or down, but with their trigonal axes collinear. The closest phenyl rings have a distance of 5.03 Å between centroids, suggesting that $\pi-\pi$ interactions play a role in the assembly.

STM images and magnetization curves $M(H)$ of Er(trensal) molecules adsorbed on G/Ir(111), G/Ru(0001), and Ru(0001) are shown in Figure 1b–d. The images taken on Er(trensal)/G reveal a complex pattern of trigonal elements exhibiting a unit

cell with lateral size of $a_{G,Ir} = 13.6 \pm 0.5$ Å and $a_{G,Ru} = 13.5 \pm 0.5$ Å for the molecules adsorbed on G/Ir(111) and G/Ru(0001), respectively. These dimensions are very similar to those found in the *ab* single-crystalline sheet of the bulk structure ($a_{bulk} = 12.95$ Å)[11] depicted in Figure 1a. The unit cells are overlaid in Figure 1b,c, facilitating the identification of the STM features. For G/Ru(0001), an additional periodic modulation appears because of the highly corrugated moiré pattern resulting from the C–Ru hybridization.[16,18] In contrast, G/Ir(111) exhibits a very weakly corrugated moiré pattern and a low degree of hybridization with the substrate. The fact that the molecular unit cell is identical on both G/Ru(0001) and G/Ir(111) indicates that the different characteristics of graphene on the two substrates do not influence the adsorption geometry and order of the molecules. According to the molecular ordering, we define the molecular coverage of one monolayer (ML) as the close-packed layer shown in Figure 1b,c, with each molecule occupying an area of ~0.8 nm^2.

In contrast to these well-ordered periodic molecular lattices, the spatial distribution of Er(trensal) molecules is completely different when the molecules are deposited directly on the bare Ru(0001) surface, as seen in Figure 1d. In that case, the molecules adsorb at random sites and do not exhibit any long-range order. Different apparent heights suggest that there are different adsorption conformations. A histogram of apparent heights is given in the (Supporting Information (SI)), together with overview STM images of the three samples presented in Figure 1.

The different adsorption behavior is reflected in the magnetization curves $M(H)$ shown in Figure 1b–d, which have been obtained from low-temperature XMCD. This technique is capable of measuring absolute values of the element specific spin and orbital magnetic moments with high sensitivity reaching down to molecular submonolayers.[39] Since XMCD measures the projection of the magnetic moment onto

the beam direction, normal and grazing incidence geometries yield information about the presence and orientation of magnetic anisotropy in the probed molecular ensemble, that is, the directional dependence of the magnetization in an applied field. Details about the X-ray measurements are given in the SI.

A striking difference is visible between the $M(H)$ curves recorded on the molecules adsorbed on G compared to direct adsorption on Ru(0001). For molecules on the bare Ru(0001) surface, $M(H)$ exhibits almost no angular dependence, consistent with the different adsorption conformations and the corresponding distribution of the molecular magnetic easy axes (cf. Figure 1d). However, on the G layers, the Er magnetic moment projected onto the surface normal is significantly stronger than the one measured in grazing geometry. This is in excellent agreement with the STM observations, showing that the C_3 axes that are collinear with the magnetic easy axes of the molecules[11] are oriented normal to the surface. Figure 1b,c reveals that in the grazing orientation the XMCD signal is about half of that observed along the surface normal, which indicates a very strong magnetic anisotropy. Hence, in grazing geometry, even the maximum employed applied field of 6.8 T is not sufficient to align the Er magnetic moments parallel to the field.

Simulated $M(H)$ curves from spin-Hamiltonian calculations shown in Figure 1b,c allow comparison of the magnetic behavior of the adsorbed molecules with the one of the bulk phase. Calculations using the spin-Hamiltonian $\hat{H}_0 = \sum_{k,q} B_k^q \hat{O}_k^q(\mathbf{J}) + g_{Er}\mu_B\mu_0 \hat{\mathbf{J}} \cdot \mathbf{H}$ with the Stevens parameters B_k^q obtained in previous work on bulk single crystals[11] (cf. SI for the details of the calculations) demonstrate that the magnetic behavior of the Er(trensal) molecules on G is identical to that of Er(trensal) in the molecular single crystal.

X-ray absorption and XMCD spectra obtained at the Er $M_{4,5}$ edges on Er(trensal) deposited on G/Ru(0001) are presented in Figure 2. The polarization-dependent XAS (Figure 2a) exhibits the typical three peaks at the Er M_5 edge that are related to transitions from the complete $3d_{5/2}$ shell to the partially filled 4f shell. The large XMCD (Figure 2b) signal indicates the presence of a strong Er magnetic moment located

in the 4f shell. The XMCD $M_{4,5}$ features have the same sign, in agreement with the sizable orbital angular momentum predicted by Hund's rules, which leads to a ground state of $^4I_{15/2}$. The angular dependence of the XMCD indicates that the Er magnetic moment is much stronger in normal than in grazing orientation, reflecting the behavior of the field-dependent magnetization $M(H)$ seen in Figure 1b,c. In addition, a more subtle difference within the three peak substructure of the Er M_5 edge is observed in the polarization-dependent XAS, as shown in Figure 2c,d. Note that the middle and right peaks associated with $\Delta J = -1$ transitions[40] are more pronounced in normal incidence, whereas the left peak ($\Delta J = 0$) is stronger in grazing incidence. Multiplet calculations[41] employing the known ligand field of the Er(trensal) molecules as described in the SI are in excellent agreement with the experimental data, confirming the similarity to the bulk magnetic properties. Using the XMCD sum rules,[42,43] absolute values of the spin m_S and orbital m_L magnetic moments can be extracted. Their application to the spectra presented in Figure 2 yields a total magnetic moment $m_S + m_L = 6.5 \pm 0.4\ \mu_B$ in normal and $4.0 \pm 0.4\ \mu_B$ in grazing incidence. For comparison, the multiplet calculations yield 6.8 μ_B and 4.1 μ_B in normal and grazing incidence, respectively, and spin-Hamiltonian calculations give 6.7 μ_B and 3.9 μ_B for the temperature and magnetic field used in the experiment. These values deduced from alternative methods agree very well. The values found for the other samples presented in this work are reported in Table S1 (SI).

The XAS and XMCD recorded at the Er M_5 peak for submonolayers and a multilayer of Er(trensal) deposited on G/Ir(111), G/Ru(0001), as well as on Ru(0001) are shown in Figure 3. The absence and presence of the angle dependence is consistent with the STM results of multiple adsorption conformations on Ru(0001) and oriented molecules on G/Ru(0001) and G/Ir(111), respectively. Interestingly, we observe no preferential orientation in the molecular multilayer on G/Ru(0001) (Figure 3c), which indicates the presence of a significant rotational disorder, that is, no orientation of the molecular C_3 axes.

The orientation and self-assembly of the molecules on the graphene layers can be understood by considering that the subtle balance between molecule–molecule and molecule–surface interactions determines the adsorption behavior. The self-assembly is driven by the lateral molecule–molecule interaction, which, in the present case, is dominated by π–π interactions between the phenyl rings. In general, lateral variations of the adsorption energy originating from the strongly corrugated moiré pattern in G/Ru(0001) can result in a template effect through the presence of preferred adsorption sites.[22,27,30,31,33,44] On weakly bound graphene exhibiting little corrugation and work function modulation, such as G/Ir(111),[23,44] G/Pt(111),[33] and G/h-BN,[25] no preferential adsorption, that is, no template effect, has been found. In the present system, the lateral molecule–molecule interaction is strong enough to override a possible template effect even on G/Ru(0001). Note that this behavior is similar to the one observed for the C_{60}/G/Ru(0001) system,[45] also containing nonplanar molecules, as in these systems molecule–surface interactions tend to be weaker than in planar molecules in the absence of specific functional groups. If the molecule–surface interaction is dominant, as in the case of direct adsorption on Ru(0001), the molecules are trapped during the deposition process. Thus, they remain at their landing positions
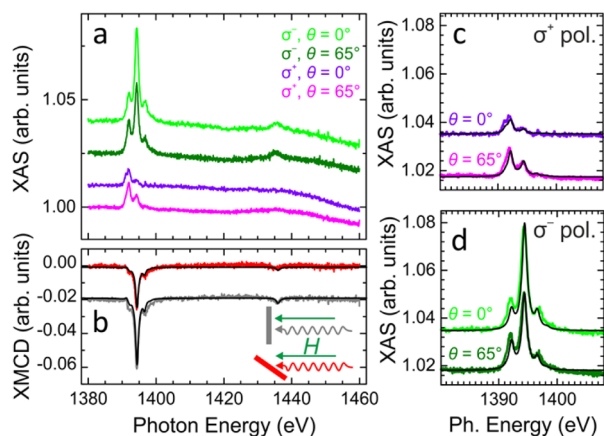
Figure 2. X-ray spectra recorded on 0.25 ± 0.03 ML Er(trensal)/G/Ru(0001) in normal ($\theta = 0°$) and grazing incidence ($\theta = 65°$) at 3 K and 6.8 T. (a) XAS and (b) XMCD. (c,d) Polarization and angle dependence at the Er M_5 edge. Solid black lines denote calculations as described in the text. Spectra in (a–d) have been offset for clarity.
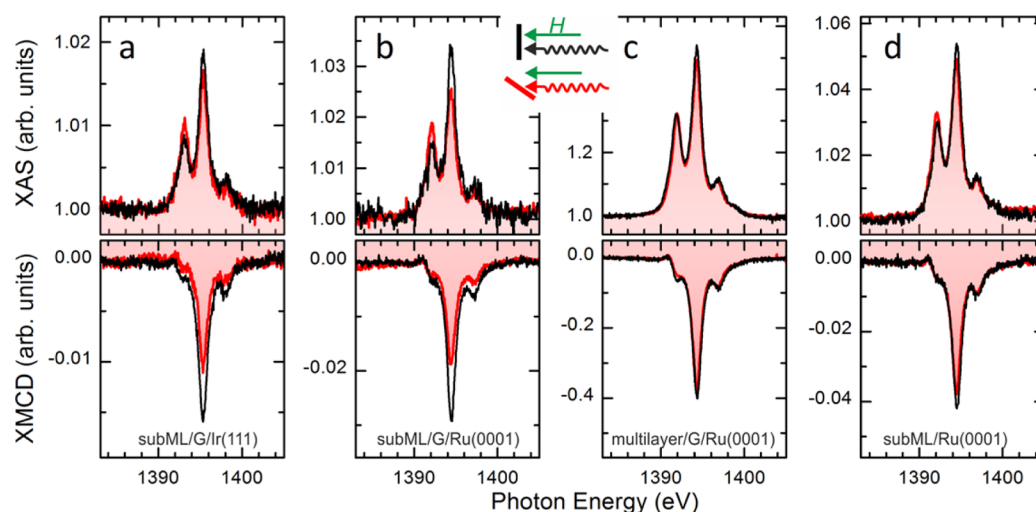
Figure 3. XAS (top panels) and XMCD (bottom panels) at the Er M_5 edge recorded in normal ($\theta = 0°$) and grazing ($\theta = 65°$) incidence of the X-rays at 3 K on the following samples: (a) 0.30 ± 0.03 ML Er(trensal)/G/Ir(111), (b) 0.25 ± 0.03 ML Er(trensal)/G/Ru(0001), (c) 3.2 ± 0.3 ML Er(trensal)/G/Ru(0001), (d) 0.30 ± 0.03 ML Er(trensal)/Ru(0001).

in a fixed conformation, unable to orient and to self-assemble into dense layers, as observed on G.

Our results suggest that in the case of weak adsorption the transferral of the Er magnetic properties from the bulk to the surface-deposited molecules is possible. This is remarkable in view of the high sensitivity of lanthanides toward minor perturbations, which can result from peripheral ligand functionalization[11] as well as from surface adsorption.[14] Our results demonstrate that engineering of the net magnetic anisotropy of a molecule−inorganic heterostructure can be achieved through G decoupling layers.

CONCLUSION

In summary, we have investigated the adsorption properties and magnetic behavior of Er(trensal) molecules on graphene/Ru(0001) and graphene/Ir(111), as well as on bare Ru(0001). STM images reveal that on Ru(0001) the molecules exhibit several adsorption conformations and random adsorption sites, hinting toward a strong molecule−surface interaction. In line with the different orientations of the magnetic easy axes of the molecules, XMCD does not detect a significant difference in the Er magnetization curve $M(H)$ between normal and grazing geometries. In contrast, submonolayers of Er(trensal) molecules on graphene/Ru(0001) and on graphene/Ir(111) are fully oriented with their easy axes normal to the substrate surface, and they form densely packed self-assembled islands. A large contrast between normal and grazing magnetization is observed in XMCD, in agreement with the out-of-plane alignment of the C_3 axes inferred from the STM studies. The molecular islands do not exhibit any preference of their azimuthal orientation with respect to the graphene. Furthermore, the corrugation of the moiré pattern of graphene/Ru(0001), which is stronger than the one of graphene/Ir(111), has no influence on the self-assembly of the molecules. Spin-Hamiltonian calculations reveal that the magnetic properties of the Er(trensal) molecules on the graphene layers are identical to those in the bulk single crystal. Our study is a direct demonstration of controlling the net magnetic anisotropy in a molecule−inorganic heterostructure. It opens a new path toward organizing nonplanar single-ion magnets on surfaces on a large scale while preserving their bulk magnetic properties,

which is of high relevance for the bottom-up design of molecule-based spintronics devices.

METHODS

Sample Preparation. Ru(0001) and Ir(111) single crystals were cleaned in ultrahigh vacuum by repeated cycles of Ar⁺ ion sputtering and annealing at a temperature of 1400 K. In order to grow the graphene layer, 100 Langmuirs of ethylene (C_2H_4) was dosed, while the substrate was held at 1400 K. Solvent-free Er(trensal), where H_3trensal = 2,2′,2″-tris(salicylideneimino)triethylamine, was synthesized according to literature procedures.[10,11] It was sublimed from a molecular effusion cell held at 560 K onto the substrates at room temperature, and the sublimation rate was measured using a quartz crystal microbalance.

X-ray Absorption Measurements. The X-ray measurements were performed at the EPFL/PSI X-Treme beamline[46] at the Swiss Light Source, Paul Scherrer Institut, Villigen, Switzerland. XAS and XMCD refer to the sum and difference of the spectra taken with the two circular polarizations of the X-rays, respectively. The quality of the graphene layers used in the X-ray studies was checked *in situ* using an STM connected to the X-Treme beamline.

Scanning Tunneling Microscopy. The surface-adsorbed molecules were studied with a home-built low-temperature STM operated at 5 K.[47]

ASSOCIATED CONTENT

Ⓢ Supporting Information

The Supporting Information is available free of charge on the ACS Publications website at DOI: 10.1021/acsnano.5b08178.

    Additional STM images, details of X-ray absorption spectroscopy, and spin-Hamiltonian calculations (PDF)

AUTHOR INFORMATION

Corresponding Author
*E-mail: jan.dreiser@psi.ch.

Present Address
¶Fachbereich Physik, Universität Konstanz, 78457 Konstanz, Germany.

Notes
The authors declare no competing financial interest.

ACKNOWLEDGMENTS

REFERENCES

(1) Caneschi, A.; Gatteschi, D.; Sessoli, R.; Barra, A. L.; Brunel, L. C.; Guillot, M. Alternating Current Susceptibility, High Field Magnetization, and Millimeter Band EPR Evidence for a Ground $S = 10$ State in $[Mn_{12}O_{12}(CH_3COO)_{16}(H_2O)_4] \cdot 2CH_3COOH \cdot 4H_2O$. *J. Am. Chem. Soc.* **1991**, *113*, 5873−5874.

(2) Sessoli, R.; Gatteschi, D.; Caneschi, A.; Novak, M. A. Magnetic Bistability in a Metal-Ion Cluster. *Nature* **1993**, *365*, 141−143.

(3) Gatteschi, D.; Sessoli, R.; Villain, J. *Molecular Nanomagnets*; Oxford University Press, 2006.

(4) Rocha, A. R.; García-suárez, V. M.; Bailey, S. W.; Lambert, C. J.; Ferrer, J.; Sanvito, S. Towards Molecular Spintronics. *Nat. Mater.* **2005**, *4*, 335−339.

(5) Sanvito, S. Molecular Spintronics. *Chem. Soc. Rev.* **2011**, *40*, 3336−3355.

(6) Joachim, C.; Gimzewski, J. K.; Aviram, A. Electronics Using Hybrid-Molecular and Mono-Molecular Devices. *Nature* **2000**, *408*, 541−548.

(7) Ishikawa, N.; Sugita, M.; Ishikawa, T.; Koshihara, S.; Kaizu, Y. Mononuclear Lanthanide Complexes with a Long Magnetization Relaxation Time at High Temperatures: A New Category of Magnets at the Single-Molecular Level. *J. Phys. Chem. B* **2004**, *108*, 11265−11271.

(8) Feltham, H. L. C.; Brooker, S. Review of Purely 4f and Mixed-Metal Nd-4f Single-Molecule Magnets Containing Only One Lanthanide Ion. *Coord. Chem. Rev.* **2014**, *276*, 1−33.

(9) Dreiser, J. Molecular Lanthanide Single-Ion Magnets: From Bulk to Submonolayers. *J. Phys.: Condens. Matter* **2015**, *27*, 183203.

(10) Flanagan, B. M.; Bernhardt, P. V.; Krausz, E. R.; Lüthi, S. R.; Riley, M. J. Ligand-Field Analysis of an Er(III) Complex with a Heptadentate Tripodal N_4O_3 Ligand. *Inorg. Chem.* **2001**, *40*, 5401−5407.

(11) Pedersen, K. S.; Ungur, L.; Sigrist, M.; Sundt, A.; Schau-Magnussen, M.; Vieru, V.; Mutka, H.; Rols, S.; Weihe, H.; Waldmann, O.; Chibotaru, L. F.; Bendix, J.; Dreiser, J. Modifying the Properties of 4f Single-Ion Magnets by Peripheral Ligand Functionalisation. *Chem. Sci.* **2014**, *5*, 1650−1660.

(12) Lucaccini, E.; Sorace, L.; Perfetti, M.; Costes, J.-P.; Sessoli, R. Beyond the Anisotropy Barrier: Slow Relaxation of the Magnetization in Both Easy-Axis and Easy-Plane Ln(trensal) Complexes. *Chem. Commun.* **2014**, *50*, 1648−1651.

(13) Perfetti, M.; Lucaccini, E.; Sorace, L.; Costes, J. P.; Sessoli, R. Determination of Magnetic Anisotropy in the LnTRENSAL Complexes (Ln = Tb, Dy, Er) by Torque Magnetometry. *Inorg. Chem.* **2015**, *54*, 3090.

(14) Dreiser, J.; Wäckerlin, C.; Ali, M. E.; Piamonteze, C.; Donati, F.; Singha, A.; Pedersen, K. S.; Rusponi, S.; Bendix, J.; Oppeneer, P. M.; Jung, T. A.; Brune, H. Exchange Interaction of Strongly Anisotropic Tripodal Erbium Single-Ion Magnets with Metallic Surfaces. *ACS Nano* **2014**, *8*, 4662−4671.

(15) Oshima, C.; Nagashima, A. Ultra-Thin Epitaxial Films of Graphite and Hexagonal Boron Nitride on Solid Surfaces. *J. Phys.: Condens. Matter* **1997**, *9*, 1.

(16) Marchini, S.; Günther, S.; Wintterlin, J. Scanning Tunneling Microscopy of Graphene on Ru(0001). *Phys. Rev. B: Condens. Matter Mater. Phys.* **2007**, *76*, 075429.

(17) Castro Neto, A. H.; Guinea, F.; Peres, N. M. R.; Novoselov, K. S.; Geim, A. K. The Electronic Properties of Graphene. *Rev. Mod. Phys.* **2009**, *81*, 109−162.

(18) Wintterlin, J.; Bocquet, M.-L. Graphene on Metal Surfaces. *Surf. Sci.* **2009**, *603*, 1841−1852.

(19) Nagashima, A.; Tejima, N.; Gamou, Y.; Kawai, T.; Oshima, C. Electronic Structure of Monolayer Hexagonal Boron Nitride Physisorbed on Metal Surfaces. *Phys. Rev. Lett.* **1995**, *75*, 3918−3921.

(20) Auwärter, W.; Kreutz, T. J.; Greber, T.; Osterwalder, J. XPD and STM Investigation of Hexagonal Boron Nitride on Ni(111). *Surf. Sci.* **1999**, *429*, 229−236.

(21) Corso, M.; Auwärter, W.; Muntwiler, M.; Tamai, A.; Greber, T.; Osterwalder, J. Boron Nitride Nanomesh. *Science* **2004**, *303*, 217−220.

(22) Roos, M.; Uhl, B.; Künzel, D.; Hoster, H. E.; Groß, A.; Behm, R. J. Intermolecular vs Molecule−substrate Interactions: A Combined STM and Theoretical Study of Supramolecular Phases on graphene/Ru(0001). *Beilstein J. Nanotechnol.* **2011**, *2*, 365−373.

(23) Hämäläinen, S. K.; Stepanova, M.; Drost, R.; Liljeroth, P.; Lahtinen, J.; Sainio, J. Self-Assembly of Cobalt-Phthalocyanine Molecules on Epitaxial Graphene on Ir(111). *J. Phys. Chem. C* **2012**, *116*, 20433−20437.

(24) Bazarnik, M.; Brede, J.; Decker, R.; Wiesendanger, R. Tailoring Molecular Self-Assembly of Magnetic Phthalocyanine Molecules on Fe- and Co-Intercalated Graphene. *ACS Nano* **2013**, *7*, 11341−11349.

(25) Järvinen, P.; Hämäläinen, S. K.; Banerjee, K.; Häkkinen, P.; Ijäs, M.; Harju, A.; Liljeroth, P. Molecular Self-Assembly on Graphene on SiO_2 and H-BN Substrates. *Nano Lett.* **2013**, *13*, 3199−3204.

(26) MacLeod, J. M.; Rosei, F. Molecular Self-Assembly on Graphene. *Small* **2014**, *10*, 1038−1049.

(27) Zhou, H.; Zhang, L.; Mao, J.; Li, G.; Zhang, Y.; Wang, Y.; Du, S.; Hofer, W. A.; Gao, H.-J. Template-Directed Assembly of Pentacene Molecules on Epitaxial Graphene on Ru(0001). *Nano Res.* **2013**, *6*, 131−137.

(28) Schulz, F.; Drost, R.; Hämäläinen, S. K.; Liljeroth, P. Templated Self-Assembly and Local Doping of Molecules on Epitaxial Hexagonal Boron Nitride. *ACS Nano* **2013**, *7*, 11121−11128.

(29) Joshi, S.; Bischoff, F.; Koitz, R.; Ecija, D.; Seufert, K.; Seitsonen, A. P.; Hutter, J.; Diller, K.; Urgel, J. I.; Sachdev, H.; Barth, J. V.; Auwärter, W. Control of Molecular Organization and Energy Level Alignment by an Electronically Nanopatterned Boron Nitride Template. *ACS Nano* **2014**, *8*, 430−442.

(30) Mao, J.; Zhang, H.; Jiang, Y.; Pan, Y.; Gao, M.; Xiao, W.; Gao, H.-J. Tunability of Supramolecular Kagome Lattices of Magnetic Phthalocyanines Using Graphene-Based Moiré Patterns as Templates. *J. Am. Chem. Soc.* **2009**, *131*, 14136−14137.

(31) Zhang, H. G.; Sun, J. T.; Low, T.; Zhang, L. Z.; Pan, Y.; Liu, Q.; Mao, J. H.; Zhou, H. T.; Guo, H. M.; Du, S. X.; Guinea, F.; Gao, H.-J. Assembly of Iron Phthalocyanine and Pentacene Molecules on a Graphene Monolayer Grown on Ru(0001). *Phys. Rev. B: Condens. Matter Mater. Phys.* **2011**, *84*, 245436.

(32) Scardamaglia, M.; Forte, G.; Lizzit, S.; Baraldi, A.; Lacovig, P.; Larciprete, R.; Mariani, C.; Betti, M. G. Metal-Phthalocyanine Array on the Moiré Pattern of a Graphene Sheet. *J. Nanopart. Res.* **2011**, *13*, 6013−6020.

(33) Yang, K.; Xiao, W. D.; Jiang, Y. H.; Zhang, H. G.; Liu, L. W.; Mao, J. H.; Zhou, H. T.; Du, S. X.; Gao, H.-J. Molecule−Substrate Coupling between Metal Phthalocyanines and Epitaxial Graphene Grown on Ru(0001) and Pt(111). *J. Phys. Chem. C* **2012**, *116*, 14052−14056.

(34) Uihlein, J.; Peisert, H.; Adler, H.; Glaser, M.; Polek, M.; Ovsyannikov, R.; Bauer, M.; Chassé, T. Strong Interaction of MnPc on Ni(111): Influence of Graphene Buffer Layer. *J. Phys. Chem. C* **2014**, *118*, 28671−28678.

(35) Scardamaglia, M.; Lisi, S.; Lizzit, S.; Baraldi, A.; Larciprete, R.; Mariani, C.; Betti, M. G. Graphene-Induced Substrate Decoupling and

Ideal Doping of a Self-Assembled Iron-Phthalocyanine Single Layer. *J. Phys. Chem. C* **2013**, *117*, 3019−3027.

(36) Kahle, S.; Deng, Z.; Malinowski, N.; Tonnoir, C.; Forment-Aliaga, A.; Thontasen, N.; Rinke, G.; Le, D.; Turkowski, V.; Rahman, T. S.; Rauschenbach, S.; Ternes, M.; Kern, K. The Quantum Magnetism of Individual Manganese-12-Acetate Molecular Magnets Anchored at Surfaces. *Nano Lett.* **2012**, *12*, 518−521.

(37) Erler, P.; Schmitt, P.; Barth, N.; Irmler, A.; Bouvron, S.; Huhn, T.; Groth, U.; Pauly, F.; Gragnaniello, L.; Fonin, M. Highly Ordered Surface Self-Assembly of Fe$_4$ Single Molecule Magnets. *Nano Lett.* **2015**, *15*, 4546−4552.

(38) Burgess, J. A. J.; Malavolti, L.; Lanzilotto, V.; Mannini, M.; Yan, S.; Ninova, S.; Totti, F.; Rolf-Pissarczyk, S.; Cornia, A.; Sessoli, R.; Loth, S. Magnetic Fingerprint of Individual Fe$_4$ Molecular Magnets under Compression by a Scanning Tunnelling Microscope. *Nat. Commun.* **2015**, *6*, 8216.

(39) van der Laan, G.; Figueroa, A. I. X-Ray Magnetic Circular dichroism—A Versatile Tool to Study Magnetism. *Coord. Chem. Rev.* **2014**, *277−278*, 95−129.

(40) Goedkoop, J. B.; Thole, B. T.; van der Laan, G.; Sawatzky, G. A.; de Groot, F. M. F.; Fuggle, J. C. Calculations of Magnetic X-Ray Dichroism in the 3d Absorption Spectra of Rare-Earth Compounds. *Phys. Rev. B: Condens. Matter Mater. Phys.* **1988**, *37*, 2086−2093.

(41) Uldry, A.; Vernay, F.; Delley, B. Systematic Computation of Crystal-Field Multiplets for X-Ray Core Spectroscopies. *Phys. Rev. B: Condens. Matter Mater. Phys.* **2012**, *85*, 125133.

(42) Carra, P.; Thole, B. T.; Altarelli, M.; Wang, X. X-Ray Circular Dichroism and Local Magnetic Fields. *Phys. Rev. Lett.* **1993**, *70*, 694−697.

(43) Thole, B. T.; Carra, P.; Sette, F.; van der Laan, G. X-Ray Circular Dichroism as a Probe of Orbital Magnetization. *Phys. Rev. Lett.* **1992**, *68*, 1943−1946.

(44) Maccariello, D.; Garnica, M.; Niño, M. A.; Navío, C.; Perna, P.; Barja, S.; Vázquez de Parga, A. L.; Miranda, R. Spatially Resolved, Site-Dependent Charge Transfer and Induced Magnetic Moment in TCNQ Adsorbed on Graphene. *Chem. Mater.* **2014**, *26*, 2883−2890.

(45) Li, G.; Zhou, H. T.; Pan, L. D.; Zhang, Y.; Mao, J. H.; Zou, Q.; Guo, H. M.; Wang, Y. L.; Du, S. X.; Gao, H.-J. Self-Assembly of C$_{60}$ Monolayer on Epitaxially Grown, Nanostructured Graphene on Ru(0001) Surface. *Appl. Phys. Lett.* **2012**, *100*, 013304.

(46) Piamonteze, C.; Flechsig, U.; Rusponi, S.; Dreiser, J.; Heidler, J.; Schmidt, M.; Wetter, R.; Calvi, M.; Schmidt, T.; Pruchova, H.; Krempasky, J.; Quitmann, C.; Brune, H.; Nolting, F. X-Treme Beamline at SLS: X-Ray Magnetic Circular and Linear Dichroism at High Field and Low Temperature. *J. Synchrotron Radiat.* **2012**, *19*, 661−674.

(47) Gaisch, R.; Gimzewski, J. K.; Reihl, B.; Schlittler, R. R.; Tschudy, M.; Schneider, W. D. Low-Temperature Ultra-High-Vacuum Scanning Tunneling Microscope. *Ultramicroscopy* **1992**, *42−44*, 1621−1626.

Supporting Information

Out-of-Plane Alignment of Er(trensal) Easy Magnetization Axes Using Graphene

Jan Dreiser,[#,†]* Giulia E. Pacchioni,[†] Fabio Donati,[†] Luca Gragnaniello,[†,¶] Alberto Cavallin,[†] Kasper S. Pedersen,[§] Jesper Bendix,[‡] Bernard Delley,[∥] Marina Pivetta,[†] Stefano Rusponi,[†] and Harald Brune[†]

[#]Swiss Light Source and [∥]Condensed Matter Theory, Paul Scherrer Institut, 5232 Villigen, Switzerland, [†]Institute of Physics, Ecole Polytechnique Fédérale de Lausanne, 1015 Lausanne, Switzerland, [§]CNRS, CRPP, UPR 8641, 33600 Pessac, France and CNRS, ICMCB, UPR 9014, 33600 Pessac, France, [‡]Department of Chemistry, University of Copenhagen, 2100 Copenhagen, Denmark.

## Contents

1. Additional STM images

Overview images taken on Er(trensal) deposited on G/Ir(111), G/Ru(0001) and Ru(0001) are shown in Figure S1. Contaminations are essentially absent. An island of Er(trensal) molecules is seen in Figure S1a on the right part of the image, covering a surface step which extends from the lower left to the middle right. In Figure S1b, the molecules also cover the entire right part of the image.

Further STM images of Er(trensal)/Ru(0001) are shown in Figure S2 along with a histogram of the observed apparent heights of the molecules. The histogram suggests the presence of two main groups of molecules. More than half of the molecules exhibit the conformation marked as '1' in Figure S2b, which can be attributed to the molecules lying on their side with azimuthal disorder. Conformation '2' exhibits a three-fold rotational symmetry suggesting that these molecules stand on their feet or lie upside down with the apical nitrogen facing the surface.
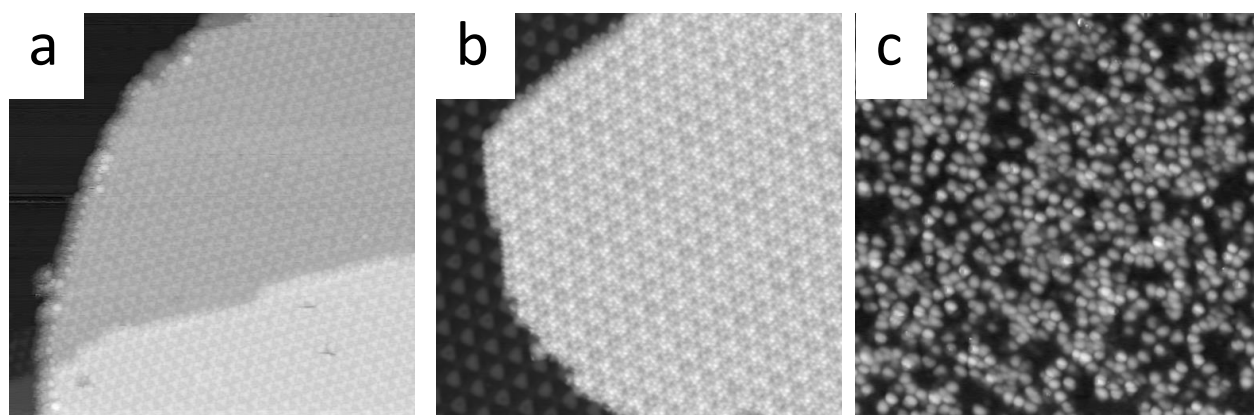
Figure S1. STM images of size 47.5×47.5 nm^2 of 0.25 ± 0.03 ML Er(trensal) deposited on (a) G/Ir(111), (b) G/Ru(0001) and (c) Ru(0001). Imaging parameters (bias voltage, tunneling current setpoint): (a) -2.5 V, 30 pA; (b) -1.0 V, 20 pA; (c) -0.2 V, 50 pA. All images were obtained at T = 5 K.
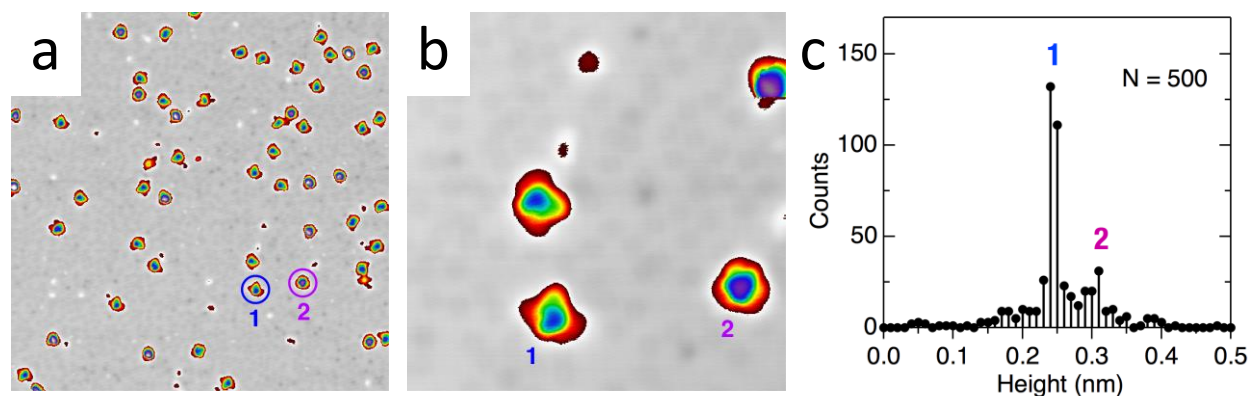
Figure S2. (a,b) STM images of 0.34 ML Er(trensal)/Ru(0001) with size (a) 38.5×38.5 nm^2 and (b) 9.5×9.5 nm^2. Imaging parameters (bias voltage, tunneling current setpoint): (a) +1.5 V, 150 pA; (b) +1.5 V, 100 pA. (c) Histogram of apparent heights, N is the total number of molecules included in the statistic.

2. Details of X-ray absorption spectroscopy

X-ray absorption measurements were performed with a spot size of ~0.5 mm^2. In order to measure magnetization curves ($M(H)$) the XAS at the edge and the pre-edge was measured in an alternating fashion while continuously ramping the magnetic field. The field sweeps were done for the two circular polarizations of the X-rays, using ramping speeds from 0.7 to 2.1 T/min.

To facilitate the comparison between normal and grazing orientations in Figure 3 of the main text, the grazing incidence XMCD spectra were scaled by a constant factor f ($0.9 < f < 1.1$) determined from the ratio of the M_5 peak areas in normal *vs*. grazing incidence.

The nominal coverage with molecules determined using a quartz microbalance was doublechecked by comparing the background-normalized area of the Er M_5 peak to a previously characterized sample of Er/Cu(111). In this procedure the different attenuation lengths of Cu, Ru and Ir relevant for the pre-edge background were taken into account.

The Er spin and orbital angular momenta as well as the total magnetic moments obtained from the XMCD sum rules[S1,S2] are shown in Table S1. The correction for the magnetic dipole contribution $<T_z>$ was performed using the correction factor given in ref. S3.

Table S1. Er spin and orbital angular momenta and total magnetic moments from sum rules.

Sample	$<L_z>/\hbar$ $\theta = 0°$	$<S_z>/\hbar$ $\theta = 0°$	$<M_z>/\mu_B$ $\theta = 0°$	$<L_z>/\hbar$ $\theta = 65°$	$<S_z>/\hbar$ $\theta = 65°$	$<M_z>/\mu_B$ $\theta = 65°$
0.25 ML Er(trensal) /G/Ir(111)	4.5 ± 0.4	1.1 ± 0.1	**6.6 ± 0.4**	2.7 ± 0.3	0.6 ± 0.1	**3.9 ± 0.4**
0.25 ML Er(trensal) /G/Ru(0001)	4.3 ± 0.4	1.1 ± 0.1	**6.5 ± 0.4**	2.7 ± 0.3	0.6± 0.1	**4.0 ± 0.4**
3 ML Er(trensal) /G/Ru(0001)	2.7 ± 0.3	0.7 ± 0.1	**4.1 ± 0.4**	2.8 ± 0.3	0.7 ± 0.1	**4.1 ± 0.4**
0.3 ML Er(trensal) /Ru(0001)	3.5 ± 0.3	0.8 ± 0.1	**5.0 ± 0.4**	3.3 ± 0.4	0.8 ± 0.1	**4.9 ± 0.4**

X-ray spectra were calculated using the multiX software.[S4] Coulomb and spin-orbit interactions were scaled to 80% and 99% of the computed values using first principles, respectively. A core-hole broadening of 0.5 eV was used to match the experimental peak width. The ligand field of the trensal ligand was parameterized by effective point charges given in Table S2, where the z axis is taken parallel to the molecular C_3 axis and the Er(III) ion is located at the origin of the coordinate system. The nominal positions of the oxygen and nitrogen atoms as obtained from the molecular structure in the bulk[S5] were used as positions of the effective point charges. The magnitudes of the effective charges located at these positions were obtained using a least-squares fit in which the known energy spectrum of the ground-state multiplet[S6] and the longitudinal component of the g-factor[S5] were used as observations. In this fit, the three parameters q_O, q_N and $q_{N,api}$ (*cf.* Table S2), were allowed to vary freely.

According to Table S2, the magnitudes of the nitrogen effective point charges are rather large. This can be understood by the fact that no displacement of the point charges relative to the atom coordinates obtained from X-ray diffraction was allowed in our model, in contrast to, *e.g.*, the procedure published in ref. S7. In order to keep the number of free parameters low, we only varied the strength of the charge in the fit.

Table S2. Effective point charges and corresponding coordinates.

	x / Å	y / Å	z / Å	q / e
O	0.7229	-1.706	-1.1639	$-0.652 = q_O$
O	1.1154	1.4801	-1.1639	$-0.652 = q_O$
O	-1.8401	0.227	-1.1639	$-0.652 = q_O$
N	2.1666	-0.5968	0.9856	$-3.612 = q_N$
N	-1.6013	-1.5779	0.9856	$-3.612 = q_N$
N	-0.5670	2.1757	0.9856	$-3.612 = q_N$
N	0	0	2.7159	$-3.603 = q_{N,api}$

3. Spin-Hamiltonian calculations

Spin-Hamiltonian calculations were carried out as described in ref. S5. Calculations were based on full diagonalization of the Hamiltonian given in equation S1.

$$\hat{H} = \sum_{k,-k \leq q \leq k} B_k^q \hat{O}_k^q(\mathbf{J}) + g_{Er}\mu_0\mu_B\hat{\mathbf{J}} \cdot \mathbf{H} \qquad \text{(Eq. S1)}$$

The first term describes the ligand field of the trensal ligand acting on the central Er(III) ion using the Stevens operator formalism with parameters B_k^q. The second, Zeeman, term represents the interaction with the applied magnetic field. Stevens parameters B_k^q and g_{Er} used in this work are identical to the previously published values.[S5]

4. References

(S1) Carra, P.; Thole, B. T.; Altarelli, M.; Wang, X. X-Ray Circular Dichroism and Local Magnetic Fields. *Phys. Rev. Lett.* **1993**, *70*, 694–697.

(S2) Thole, B. T.; Carra, P.; Sette, F.; van der Laan, G. X-Ray Circular Dichroism as a Probe of Orbital Magnetization. *Phys. Rev. Lett.* **1992**, *68*, 1943–1946.

(S3) Teramura, Y.; Tanaka, A.; Thole, B. T.; Jo, T. Effect of Coulomb Interaction on the X-Ray Magnetic Circular Dichroism Spin Sum Rule in Rare Earths. *J. Phys. Soc. Jpn.* **1996**, *65*, 3056–3059.

(S4) Uldry, A.; Vernay, F.; Delley, B. Systematic Computation of Crystal-Field Multiplets for X-Ray Core Spectroscopies. *Phys. Rev. B* **2012**, *85*, 125133.

(S5) Pedersen, K. S.; Ungur, L.; Sigrist, M.; Sundt, A.; Schau-Magnussen, M.; Vieru, V.; Mutka, H.; Rols, S.; Weihe, H.; Waldmann, O.; Chibotaru, L. F.; Bendix, J.; Dreiser, J. Modifying the Properties of 4f Single-Ion Magnets by Peripheral Ligand Functionalisation. *Chem. Sci.* **2014**, *5*, 1650–1660.

(S6) Flanagan, B. M.; Bernhardt, P. V.; Krausz, E. R.; Lüthi, S. R.; Riley, M. J. Ligand-Field Analysis of an Er(III) Complex with a Heptadentate Tripodal N_4O_3 Ligand. *Inorg. Chem.* **2001**, *40*, 5401–5407.

(S7) Baldoví, J. J.; Borrás-Almenar, J. J.; Clemente-Juan, J. M.; Coronado, E.; Gaita-Ariño, A. Modeling the Properties of Lanthanoid Single-Ion Magnets Using an Effective Point-Charge Approach. *Dalton Trans.* **2012**, *41*, 13705–13710.